Performance and stability analysis of all-perovskite tandem photovoltaics in light-driven electrochemical water splitting

Junke Wang[1,2,†], Bruno Branco[1,†], Willemijn H. M. Remmerswaal[1], Shuaifeng Hu[2], Nick R. M. Schipper[1], Valerio Zardetto[3], Laura Bellini[1], Nicolas Daub[1], Martijn M. Wienk[1], Atsushi Wakamiya[4], Henry J. Snaith[2], René A. J. Janssen[1,5]*

[1]Molecular Materials and Nanosystems, Institute of Complex Molecular Systems, Eindhoven University of Technology, partner of Solliance, P.O. Box 51, 5600 MB, Eindhoven, The Netherlands

[2]Clarendon Laboratory, Department of Physics, Parks Road, Oxford OX1 3PU, United Kingdom

[3]TNO, partner in Solliance, High Tech Campus 21, 5656 AE Eindhoven, The Netherlands

[4]Institute for Chemical Research, Kyoto University, Gokasho, Uji, Kyoto 611-0011, Japan

[5]Dutch Institute for Fundamental Energy Research, De Zaale 20, 5612 AJ Eindhoven, The Netherlands

*Email: r.a.j.janssen@tue.nl

[†]These authors contributed equally

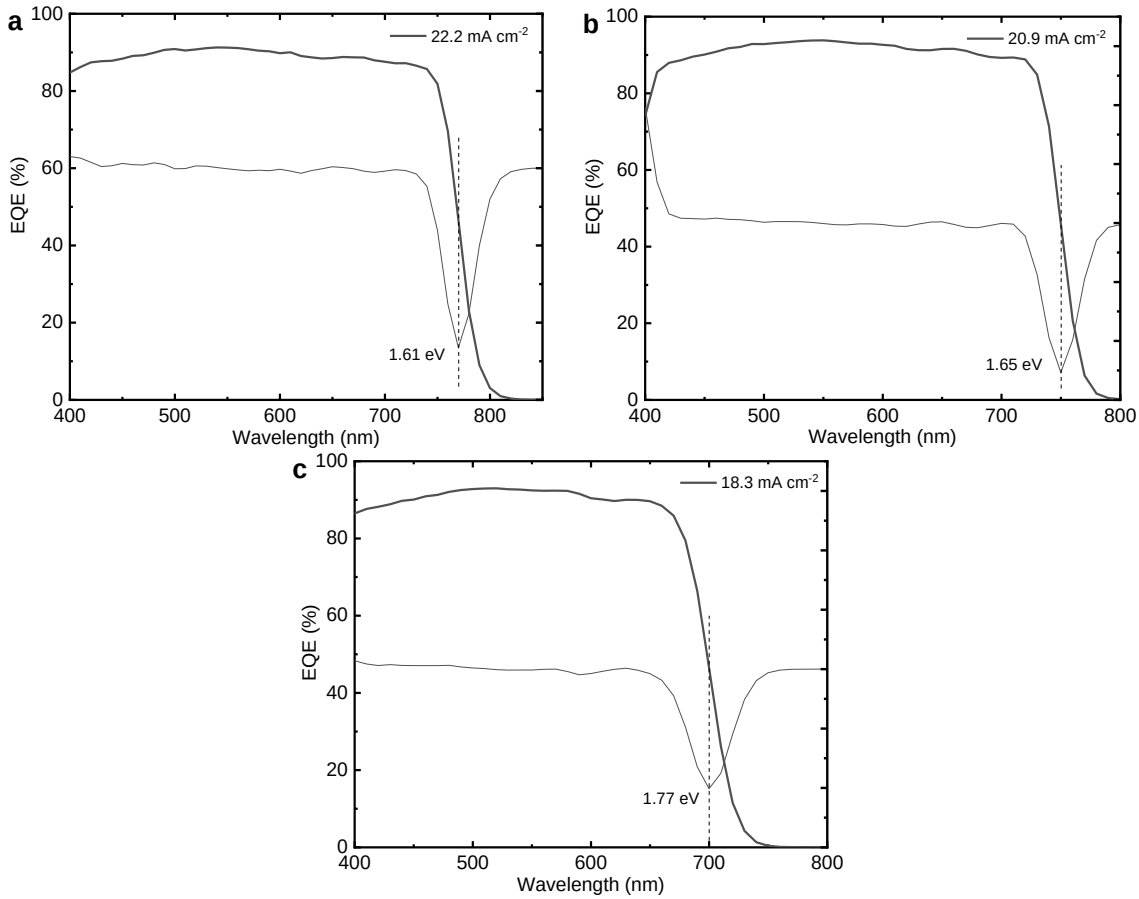

Supplementary Figure 1. EQE spectra. The EQE and its first derivative as a function of photon energy of **a**, 1.61, **b**, 1.65, and **c**, 1.77 eV PSCs. Source data are provided as a Source Data file.

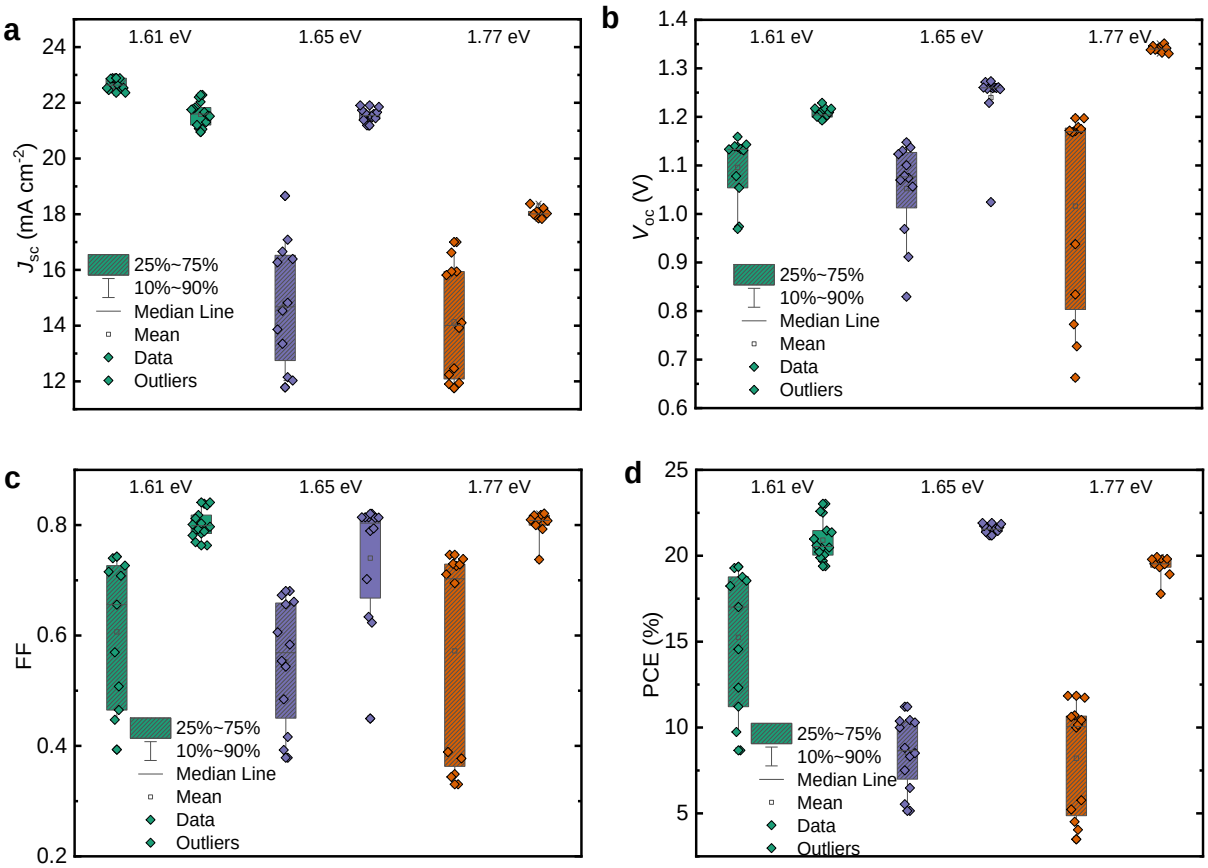

Supplementary Figure 2. Photovoltaic performance of 1.61, 1.65, and 1.77 eV bandgap PSCs (0.25 cm^2). PV parameters (reverse scans) of devices without and with surface passivation. **a**, Short-circuit current density (J_{SC}). **b**, Open-circuit voltage (V_{OC}). **c**, Fill factor (FF). **d**, Power conversion efficiency (PCE). For each variation at least 10 devices from 2 different substrates were shown. In the boxplots, the mean (open square), median (center line), 25th and 75th percentiles (box limits), minimum (–) and maximum (+), outliers (△), and 10th and 90th percentiles (whiskers) are shown. Source data are provided as a Source Data file.

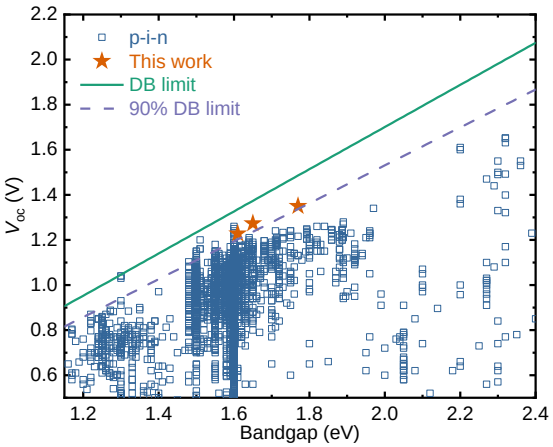

Supplementary Figure 3. Bandgap-dependent *V*OC for p–i–n single-junction PSCs. The cell data were acquired from an open-access perovskite database[1]. In the plot, the DB (detailed balance) limit (solid line), 90% of the DB limit (dashed line), the highest *V*OC of this work (solid star) and open-source data (open brackets) are shown. Source data are provided as a Source Data file.

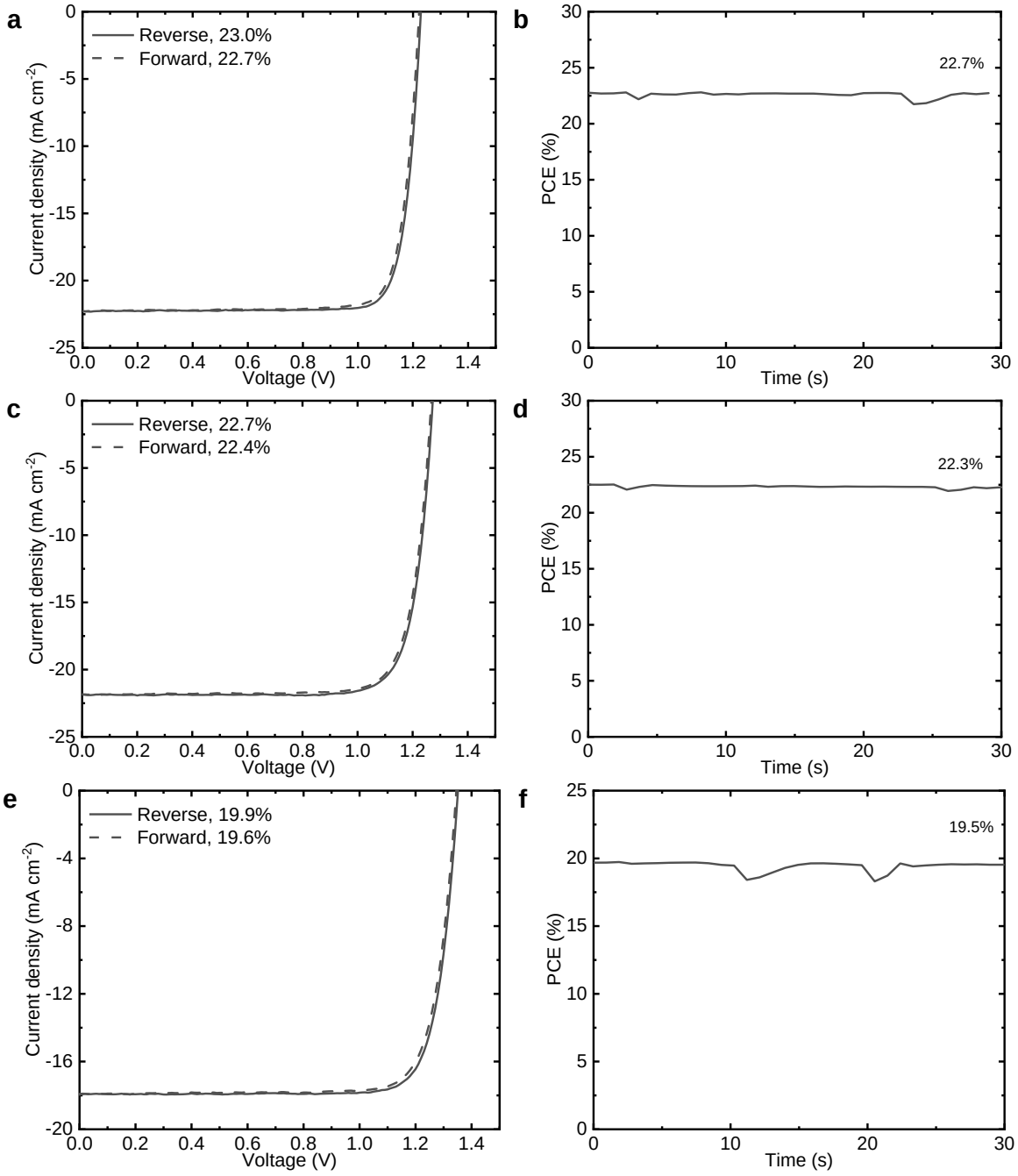

Supplementary Figure 4. Photovoltaic performance of single-junction PSCs (0.25 cm^2). *J–V* curves (reverse and forward) and maximum power point tracking of (**a**,**b**) 1.61 eV (**c**,**d**) 1.65 eV, and (**e**,**f**) 1.77 eV PSCs. Source data are provided as a Source Data file.

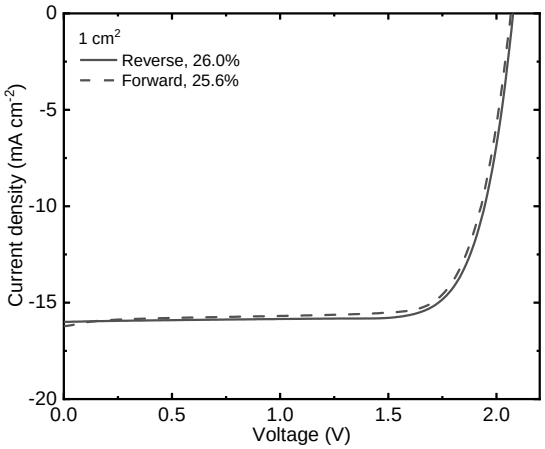

Supplementary Figure 5. Photovoltaic performance of all-perovskite tandem PSCs. *J*–*V* curves (reverse and forward) of 1 cm^2 all-perovskite tandem solar cells. Source data are provided as a Source Data file.

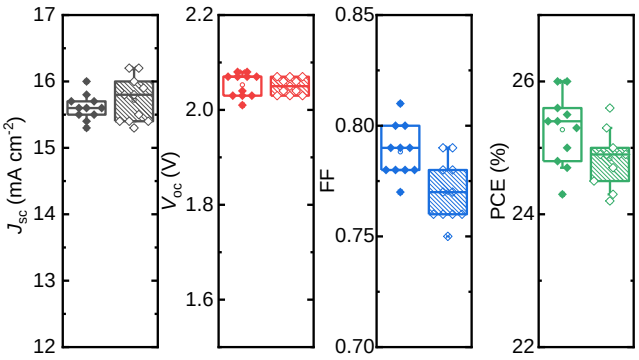

Supplementary Figure 6. Photovoltaic performance of all-perovskite tandem solar cells. PV parameters (reverse and forward scans) of 11 tandem devices fabricated on 11 different IOH substrates (1 cm^2). In the boxplots, the mean (open square), median (center line), 25th and 75th percentiles (box limits), minimum (–) and maximum (+), outliers (△), and 10th and 90th percentiles (whiskers) are shown. Source data are provided as a Source Data file.

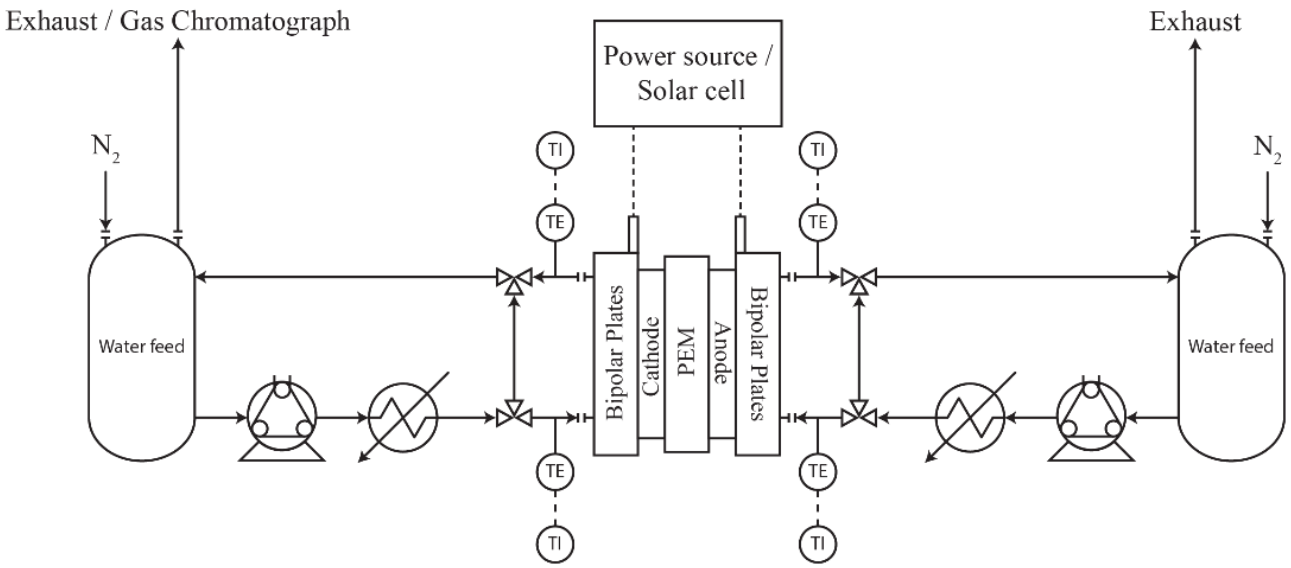

Supplementary Figure 7. Diagram of the proton exchange membrane water electrolysis setup. The feed water (ρ > 18 MΩ cm) is bubbled with N_2 gas to promote removal of evolved gases and avoid dissolution of atmospheric CO_2. The water is pumped by a peristaltic pump at a rate of 10 mL min^{-1}. The evolved gases and water are recirculated to feeding bottles, where the gases are released to the atmosphere. The hydrogen line is connected to a compact gas chromatograph CGC 4.0 (Global Analyzer Solutions–Interscience B.V.). Experiments were performed at room temperature, but the set-up allows for temperature-controlled experiments. For that purpose, the water feed passes a home–built serpentine heater immersed in an oil bath before it reaches the cell. The water inlet temperature control is provided by the oil bath. Thermocouples (TE) with temperature indicators (TI) are placed at both inlets and outlets of the cell. The lines between the heater and the cell inlet and outlets are wrapped in glass fiber tape to decrease heat loss. A by–pass between the inlets and outlets at each side of side allows preheating the feed water while the electrolysis cell is disconnected from the setup.

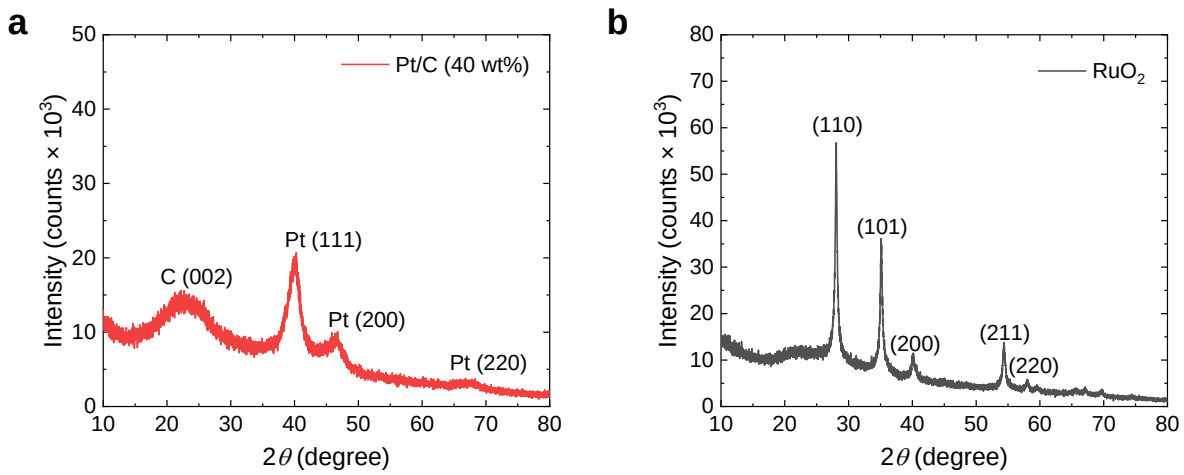

Supplementary Figure 8. X-ray diffractograms of hydrogen (Pt/C) and oxygen (RuO_2) evolution catalysts. a, Pt/C showing diffraction peaks at 40°, 46°, and 68° corresponding to the (111), (200), and (220) planes of Pt in the face centered cubic (fcc) structure (space group $Fm\bar{3}m$), in agreement with powder diffraction file no. 04-0802 of the International Centre for Diffraction Data (ICDD). The broad peak at $2\theta \approx 23°$ is assigned to amorphous carbon. **b,** RuO_2 showing diffraction peaks at 28.1°, 35.1°, 40.0°, 54.4°, and 58.0° corresponding to the (110), (101), (200), (211), and (220) reflections of RuO_2 in a tetragonal crystallographic structure (space group $P4_2/mnm$) in agreement with ICDD file 00–040-1290. Samples were prepared on glass substrates. Source data are provided as a Source Data file.

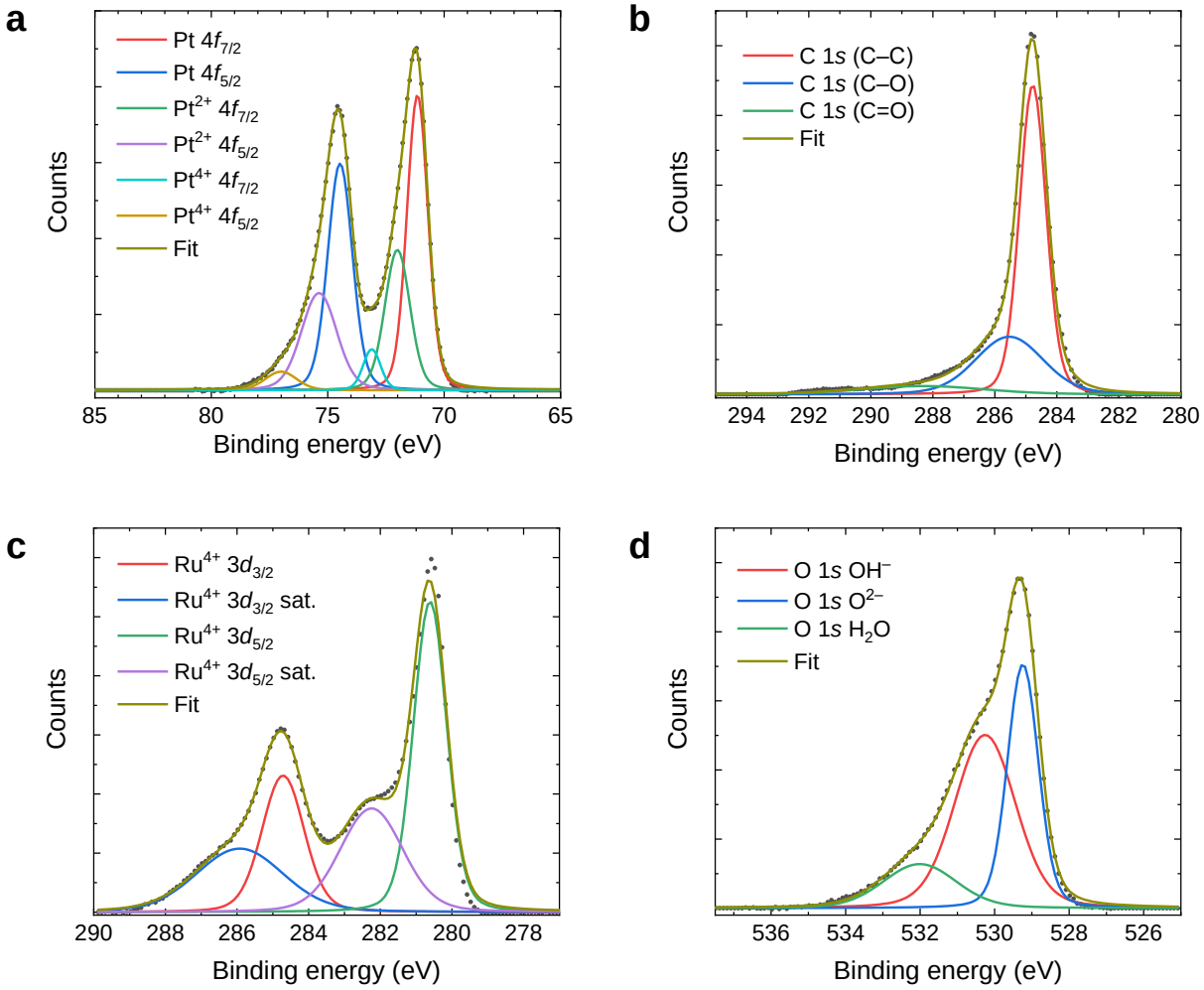

Supplementary Figure 9. X-ray photoelectron spectra of hydrogen (Pt/C) and oxygen (RuO_2) evolution catalysts. a, Pt 4*f* spectra for Pt/C. **b**, C 1*s* spectra for Pt/C. **c,** Ru 3*d* spectra for RuO_2. **d,** O 1*s* spectra for RuO_2. The experimental data is represented with solid circles and the fits with olive solid lines. Samples were prepared on glass substrates. Source data are provided as a Source Data file.

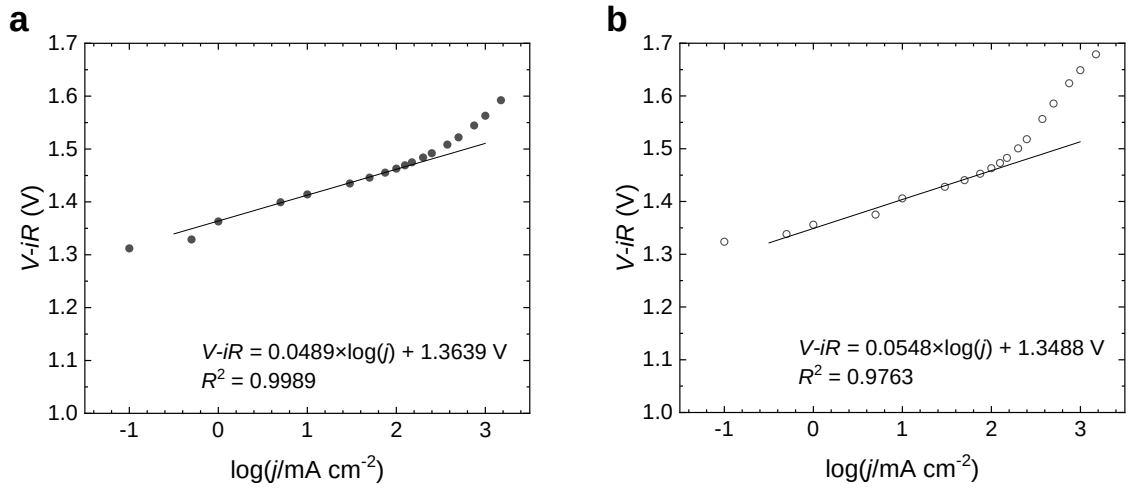

Supplementary Figure 10. Tafel plots. *iR*–free Tafel plots of the membrane electrode assembly (MEA) with Ti and C porous transport layers (PTLs) constructed from the polarization curves presented in Fig. 3a. **a**, Before operation. **b**, After continuous 192 h operation. The experimental data is represented with circles and linear fits to the data in the range from 1 to 100 mA cm^{-2} with solid lines. The Tafel slopes in the relevant region are 48.9 and 54.8 mV dec^{-1}. Source data are provided as a Source Data file.

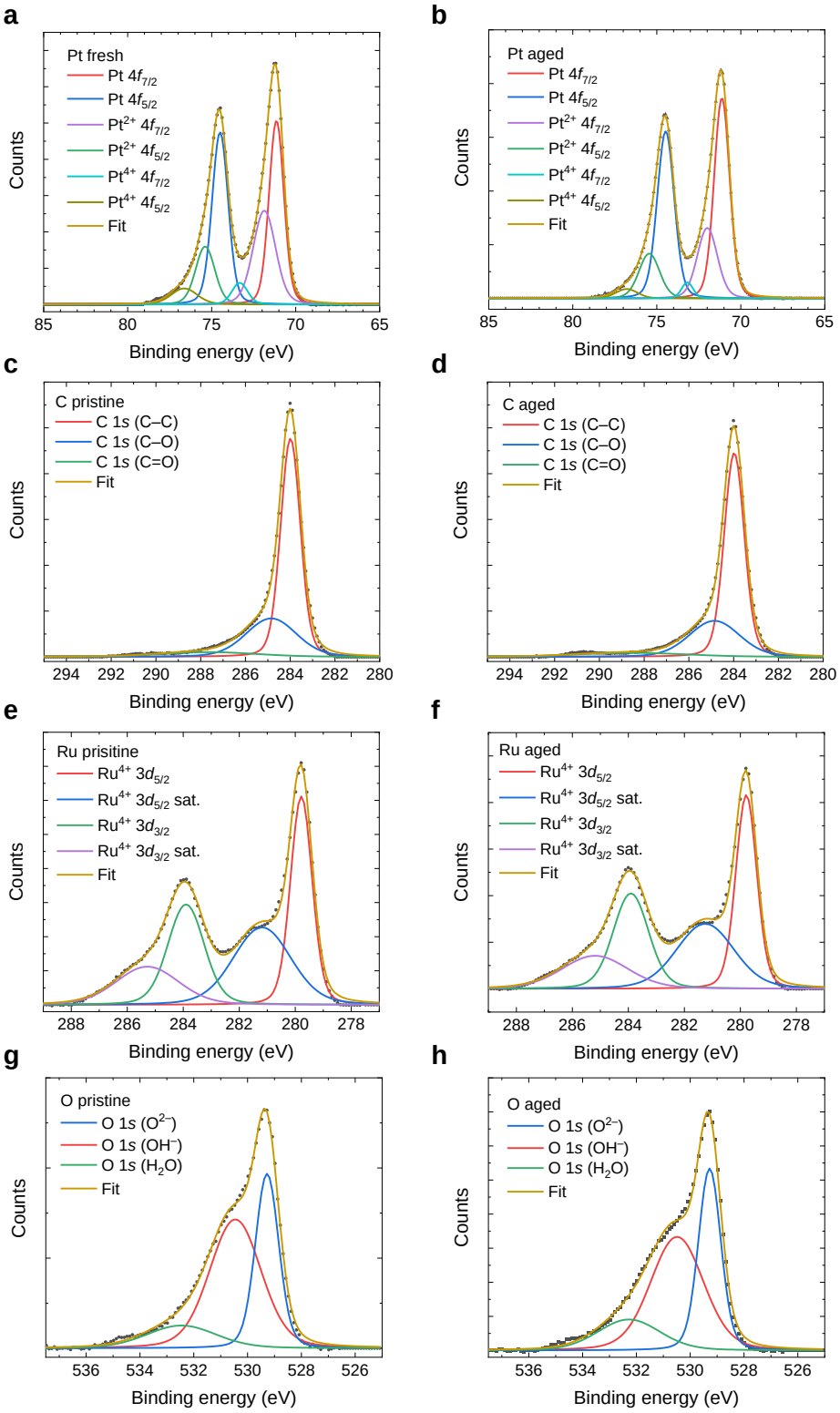

Supplementary Figure 11. X-ray photoelectron spectra of hydrogen (Pt/C) and oxygen (RuO_2) evolution catalysts on a Nafion membrane before (pristine) and after 190 h (aged) of water splitting. a, Pt 4*f* spectra for pristine Pt/C. **b**, Pt 4*f* spectra for aged Pt/C. **c**, C 1*s* spectra for pristine Pt/C. **d**, C 1*s* spectra for aged Pt/C. **e**, Ru 3*d* spectra for pristine RuO_2. **f**, Ru 3*d* spectra for aged RuO_2. **g**, O 1*s* spectra for pristine RuO_2. **h**, O 1*s* spectra for aged RuO_2. The experimental data is represented with solid circles and the fits with olive solid lines. Source data are provided as a Source Data file.

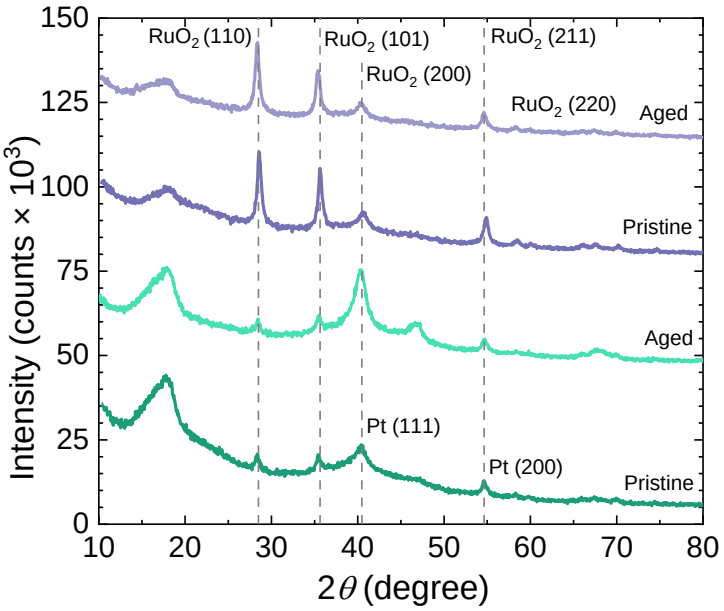

Supplementary Figure 12. X-ray diffractograms of hydrogen (Pt/C) and oxygen (RuO_2) evolution catalysts on either side of the Nafion membrane before (pristine) and after 190 h (aged) of water splitting. RuO_2 shows diffraction peaks corresponding to the (110), (101), (200), (211), and (220) reflections. Pt/C shows diffraction peaks corresponding to the (111) and (200) planes of Pt. The broad diffraction peaks at $2\theta < 20°$ are assigned to the ionomer. Note that X-ray diffraction peaks of the RuO_2 catalyst also appear at the side of the Pt/C catalyst due to X-rays passing the membrane. Supplementary Fig. 8 shows the X-ray diffractograms of the individual catalysts on glass. Source data are provided as a Source Data file.

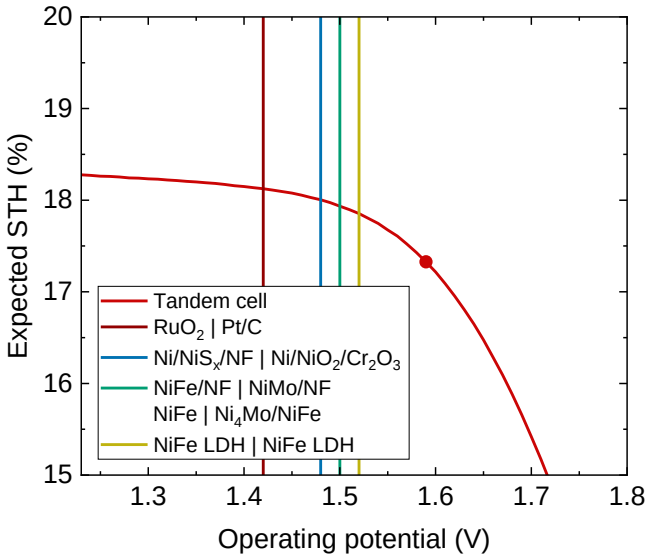

Supplementary Figure 13. Expected solar-to-hydrogen (STH) conversion efficiency vs. operating potential (V_{OP}) using the all-perovskite tandem solar cell. The vertical lines are drawn for different oxygen and hydrogen evolution catalysts combinations for which V_{OP} has been reported. The leftmost line is for the RuO_2 | Pt/C combination used here. The others are taken from the literature, from left to right: blue line (1.48 V) from Ref: 2; green line (1.50 V) from Refs: 3,4; yellow line (1.52 V) from Ref: 5. Abbreviations used are NF for nickel foam and LDH for layer double hydroxide. Source data are provided as a Source Data file.

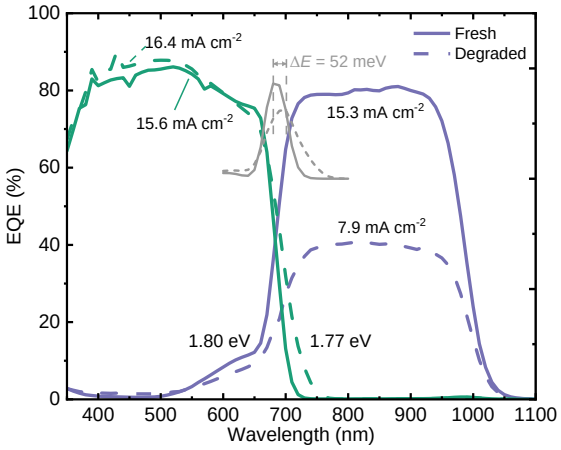

Supplementary Figure 14. EQE spectra. The EQE spectra of wide- and narrow-bandgap sub-cells in fresh (solid lines) and aged (dashed lines) all-perovskite tandem solar cells. The J_{SC} was obtained by integrating with the AM 1.5G spectrum. A redshift in the EQE onset (ΔE = 52 meV) was determined using the peak position of the first-order derivative of the EQE curves of fresh (grey solid line) and degraded (grey dashed line) wide-bandgap sub-cells. Source data are provided as a Source Data file.

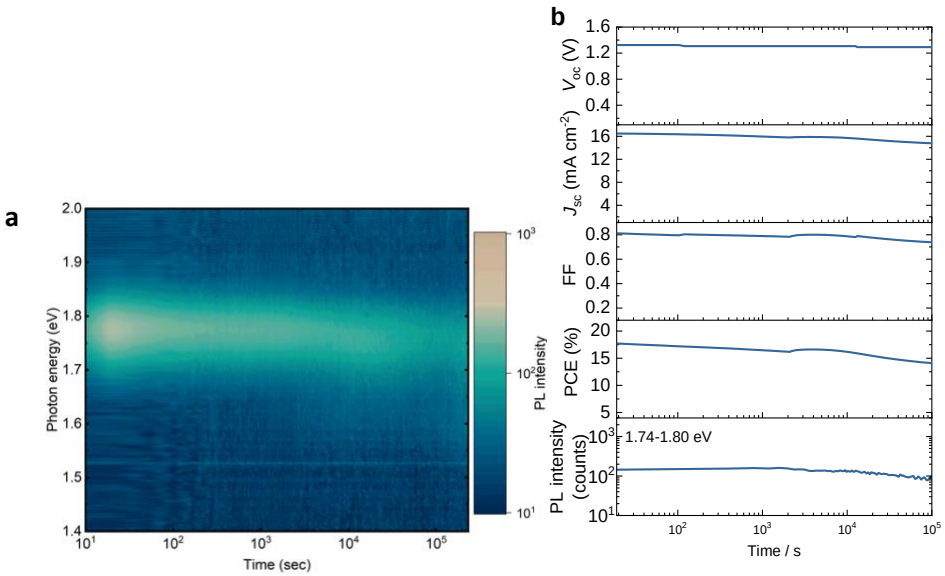

Supplementary Figure 15. Photostability and performance of 1.77 eV wide-bandgap PSCs during in situ PL and *J–V* measurements. a, Time-resolved PL intensity of a 1.77 eV PSC under a 530 LED illumination at one-sun equivalent intensity and V_{OC} conditions (following our previously developed protocol[6]). **b**, Evolution of the PV parameters (V_{OC}, J_{SC}, FF, and PCE under reverse scans) and the PL intensity counts of 1.74–1.80 eV under illumination. Source data are provided as a Source Data file.

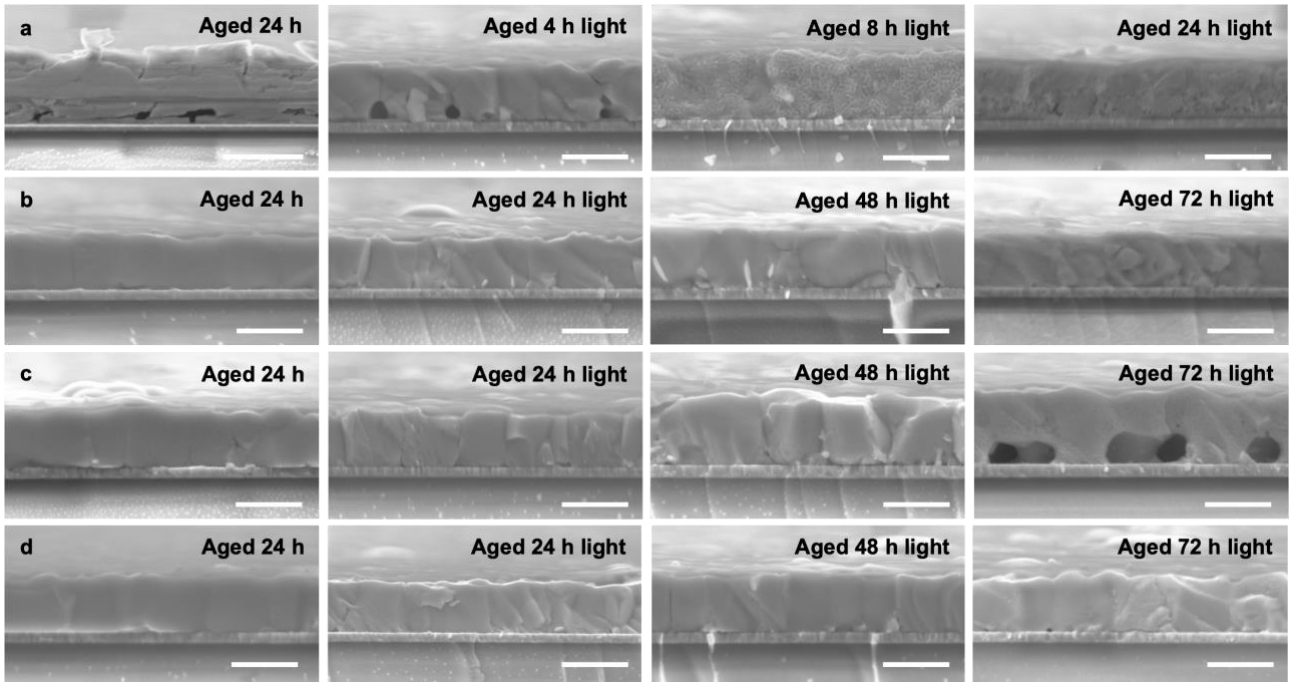

Supplementary Figure 16. Morphology of narrow-bandgap perovskites on different HTLs. a, SEM cross section images of narrow-bandgap perovskite films on PEDOT:PSS annealed at 85 °C in the dark for 24 hours and 85 °C under 1 sun illumination for 4 hours, 8 hours, and 24 hours (from left to right), respectively. Narrow-bandgap perovskite films annealed at 85 °C in the dark for 24 hours and 85 °C under 1 sun illumination for 24 hours, 48 hours, and 72 hours (from left to right), respectively. **b**, same on PTAA. **c**, same on bare ITO. **d**, same on MeO-2PACz. We note that for films processed on PEDOT:PSS, the integrity of grain boundaries started to decline under the aging conditions for more than 8 hours. This is unseen for films deposited on PTAA and bare ITO, where degradation only occurs after aging until 72 hours. Interestingly, for the perovskite processed on MeO-2PACz, no distinct changes in the morphology were seen during the measurements. The results confirm an accelerated degradation process for narrow-bandgap perovskites on PEDOT:PSS and that MeO-2PACz remains the most stable HTL during the aging tests.

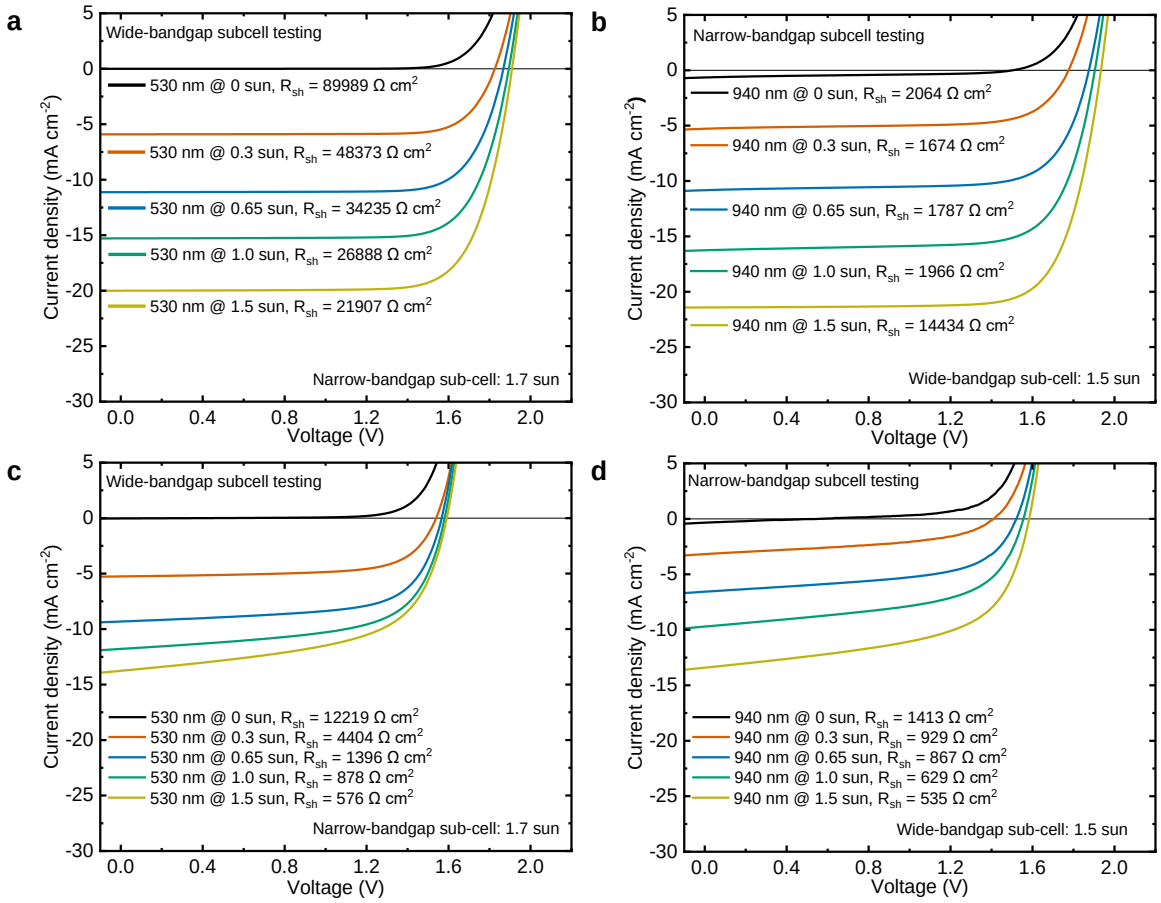

Supplementary Figure 17. Photovoltaic performance of all-perovskite tandem solar cells. *J–V* characteristics (reverse scans) of **a**, **b**, fresh and **c**, **d**, degraded tandem solar cells under different light biasing conditions. The shunt resistance was determined from the slope of the *J–V* curves near short circuit. First, single infrared (940 nm at 1.7-sun equivalent intensity) and green (530 nm at 1.5-sun equivalent illumination) LEDs were used to bias the narrow- (**a**, **c**) and wide-bandgap (**b**, **d**) sub-cells, respectively. The corresponding limiting wide- and narrow-bandgap sub-cells were then illuminated by green and infrared lights at 0, 0.3, 0.65, 1.0, and 1.5 suns while measuring the *J–V* characteristics. We note that a small aperture of 0.0314 cm^2 was used to increase the uniformity of the LED lights. This area is significantly smaller than the active area (0.16 cm^2), resulting in a lower V_{OC} due to larger dark currents. Source data are provided as a Source Data file.

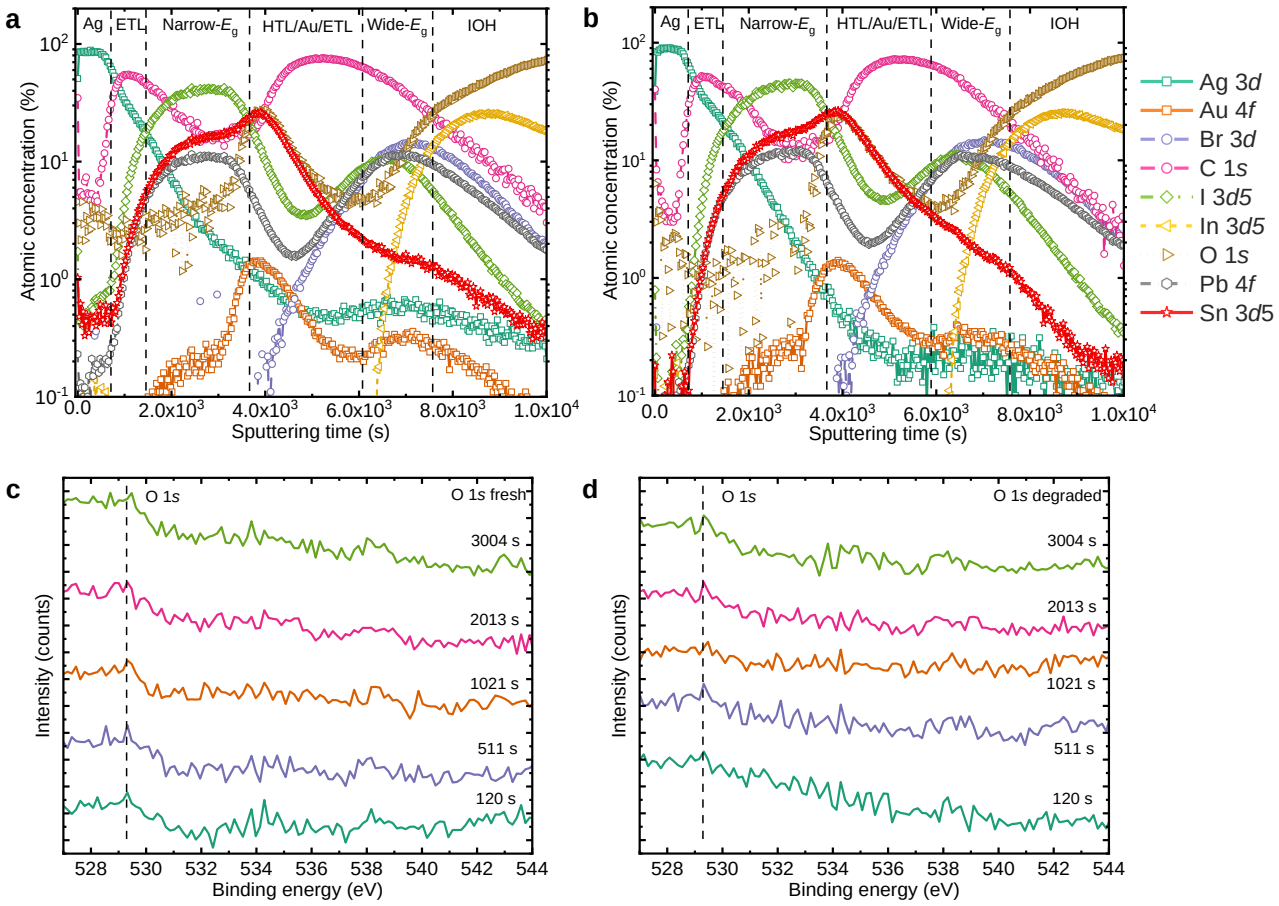

Supplementary Figure 18. Composition of all-perovskite tandem solar cells. XPS depth profiles of **a**, fresh, and **b**, degraded tandem solar cells. The O 1*s* core level of **c**, fresh, and **d**, degraded tandem solar cells measured during sputtering experiments. Source data are provided as a Source Data file.

The dashed vertical lines are guides to show the interfaces of different contact layers in tandem devices. We note that the interfaces are determined when the concentration of characteristic atoms increases to about 50% of their peak values. We also note that residues after ion-gun sputtering (such as Ag) can cause an increase of signal in the subsequent layers, leading to a longer decay in the compositional profile. There is no evidence of Ag migration in the cross-sectional SEM images for both tandem devices. Therefore, we only consider ion migration when considerable atomic signals are already found in the layers on top.

The initial atomic concentrations of O, C, Pb, Sn, and I are marginally (within 1–2%) higher in the fresh device compared to the aged device. For oxygen, the fresh narrow-bandgap sub cell should not contain any oxygen until the HTL, and we presume that oxygen can be introduced when transferring the samples from N_2 to the ambient before loading into the XPS spectrometer. We also note that the S/N ratio of O 1*s* spectra is very low during the sputtering experiments (panels **c** and **d**), making a quantitative analysis of the oxygen atomic concentration difficult.

Also, during the sputtering experiment, the sample was removed layer-by-layer by an argon ion etching gun, which created a large crater region of ~2 × 4 mm^2. This may include surface regions outside the Ag top electrode. The sputtering ions can introduce a redistribution of atoms in the surface region due to atomic mixing and knock-on implantation next to the enrichment of elements in multi-component materials due to preferential sputtering and roughness formation[7,8]. In this scenario, the atomic signals such as C, Pb, Sn and I from the underlying BCP, C_{60}, and Sn–Pb perovskite layers can be seen slightly increased at the start of the XPS experiment.

While these artifacts may hinder a detailed quantitative analysis, the strong similarity between XPS depth profiling experiments before and after ageing for all relevant atomic species indicates that the tandem device mostly retained its structural integrity without a significant redistribution of elements.

Supplementary Table 1. Average QFLS (μ) and standard deviation (σ) of perovskite films with varying bandgaps from 1.61 to 1.77 eV. All the films were processed on an HTL (ITO/NiO_x/Me-4PACz). Depending on the conditions, some samples were post-treated with a $PDAI_2$ solution and covered by PCBM (for 1.65 and 1.77 eV) and C_{60} (1.61 eV).

Half-stacks	Without ETL		With ETL		Difference	Device
	μ (meV)	σ (meV)	μ (meV)	σ (meV)	$\mu_{\text{no-ETL}} - \mu_{\text{ETL}}$ (meV)	V_{OC} (V)
1.61 eV pristine	1192	0.9	1144	2.1	48	1.16
1.61 eV with passivation	1210	3.2	1208	2.3	2	1.22
1.65 eV pristine	1246	1.8	1183	2.5	63	1.14
1.65 eV with passivation	1278	0.4	1296	0.7	−18	1.27
1.77 eV pristine	1295	15.0	1174	10.0	121	1.22
1.77 eV with passivation	1337	7.0	1293	8.0	44	1.35

Supplementary Table 2. Pseudo-*JV* parameters of narrow- and wide-bandgap perovskites obtained from neat films and sub-cells in tandem. The tandem pseudo-*JV* curves are obtained by summing the corresponding single-junction pseudo-*JV* curves. Note that the J_{SC} of both sub-cells are normalized to 16.0 mA cm^{-2} to simulate the standard *J*–*V* measurement.

Tandem cells		J_{SC} (mA cm^{-2})	V_{OC} (V)	FF	PCE (%)
Narrow-bandgap	Neat film	16.0	0.88	0.837	11.8
	Sub-cell	16.0	0.84	0.821	11.0
Wide-bandgap	Neat film	16.0	1.30	0.886	18.4
	Sub-cell	16.0	1.29	0.853	17.6
Tandem	Neat film	16.0	2.18	0.870	30.3
	Sub-cell	16.0	2.13	0.844	28.8

Supplementary Table 3. Overview of reported unbiased solar-driven PV-EC and PEC systems that use perovskite light absorbers.

Reference	Type [a]	Electrolyte	PV area [b] (cm^2)	EC area [c] (cm^2)	B/F [d]	STH [e] (%)	Durability	V_{OC} (V)
Two series connected single-junction perovskite cells								
Science **345**, 1593–1596 (2014)	PV-EC	1 M NaOH	0.318	~5	B	12.3	2 h [f]	2.00
PNAS **116**, 6624–6629 (2019)	PV-EC	Seawater	0.24	1	B	11.9	20 h	2
ACS Appl. Mater. Interfaces **12**, 55856–55864 (2020)	PV-EC	1 M PBS (pH 7)	0.18	1.87 1.50	B	13.2[g]	2 h [f]	2.1
ChemSusChem **15**, e202102471 (2022)	PV-EC	1 M KOH	0.50	0.50	B	12.67	t_{50} = 17 h	2.29
Nat. Commun. **14**, 3797 (2023)	PEC PA+PC	0.5 M H_2SO_4	0.24	n.r.[h]	B	13.4	5 h	2.23
Nat. Energy **9**, 272–284 (2024)	PEC PA	1 M KOH	0.50	0.25	B	9.8	14 h	2.32
Nat. Energy **9**, 272–284 (2024)	PEC PA	1 M KOH	15.36	7.68	B	8.9	4 h	2.32
Single-junction perovskite cell								
ChemSusChem **16**, e202201689 (2023)	PV-EC	0.5 M H_2SO_4 2 M NaOH	1	1	B	14.4	~1100 s [f]	1.13
Two-terminal (monolithic) perovskite-organic tandem cells								
Adv. Energy Mater. **10**, 2000361 (2020)	PV-EC	1 M KOH	0.13	n.r.[h]	B	12.3	55 min	1.85
Four-terminal perovskite-silicon tandem cells								
Adv. Energy Mater. **10**, 2000772 (2020)	PEC PC	1 M H_2SO_4	0.3	0.3	B	17.6	400 s	1.82
Adv. Energy Mater. **11**, 2101053 (2021)	PV-EC	1 M KOH	1	2	B	20.01	15 h	1.92
Two-terminal (monolithic) perovskite-silicon tandem cells								
ACS Appl. Mater. Interfaces **11**, 33835–33843 (2019)	PV-EC	1 M KOH	0.1875	2	B	17.52	200 s [f]	1.7
Joule **3**, 2930–2941 (2019)	PV-EC	1 M KOH	1.42	1.42	B	18.7	2 h	1.76
Sol. RRL **6**, 2100748 (2022)	PV-EC	0.5 M H_2SO_4	0.5091	4	B	19.68	10 h [f]	1.85
Adv. Mater. Technol. **8**, 2201131 (2023)	PV-EC	mQ H_2O	1	4	F	21.5	54 h [f]	1.80
Nat. Commun. **14**, 3797 (2023)	PEC PA	0.5 M H_2SO_4	0.44	n.r.[h]	B	20.8	t_{60} = 102 h	1.90
Four-terminal perovskite-perovskite tandem cells								
ACS Energy Lett. 7, 4215–4223 (2022)	PV-EC	1 M KOH	0.1	n.r.[h]	B	13.1	$t_{97.2}$ = 1 h [f]	2.13
Two-terminal (monolithic) perovskite-perovskite tandem cells								
ACS Energy Lett. **8**, 2611–2619 (2023)	PEC PC	0.5 M H_2SO_4	1	1	B	15.0	t_{95} = 120 h	2.104
This work	PV-EC	mQ H_2O	1	1	F	17.8	t_{60} = 184 h	2.08

[a] PV-EC: separate PV and EC cells. PEC: integrated PV and EC cells with either photoanode (PA) or photocathode (PC). [b] Total active area of solar cell. [c] Area per electrode. [d] B = batch electrochemical cell, F = flow electrochemical cell. [e] At 1 Sun intensity. [f] Total exposure time during chopped or interrupted illumination. [g] At 0.29 Sun intensity. [h] Not reported.

Supplementary Table 4. Pseudo-*JV* parameters of degraded narrow- and wide-bandgap perovskite sub-cells in a tandem. The tandem pseudo-*JV* curves are obtained by summing the corresponding single-junction pseudo-*JV* curves. Note that the J_{SC} of both sub-cells are normalized to 16.0 mA cm^{-2} to simulate the standard *J*–*V* measurement.

Tandem cells		J_{SC} (mA cm^{-2})	V_{OC} (V)	FF	PCE (%)
Narrow-bandgap	Fresh	16.0	0.84	0.821	11.0
	Degraded	16.0	0.79	0.828	10.5
Wide-bandgap	Fresh	16.0	1.29	0.853	17.6
	Degraded	16.0	1.30	0.850	17.6
Tandem	Fresh	16.0	2.13	0.844	28.8
	Degraded	16.0	2.09	0.849	28.3

Supplementary Table 5. Shunt resistance (kΩ cm^2) determined from fresh and aged all-perovskite tandem solar cells using sub-cell selective *J–V* measurements.

Tandem cells	530 nm (sun)	0	0.3	0.65	1.0	1.5
Wide-bandgap sub-cell testing (940 nm 1.7 suns)	Fresh	90.0	48.4	34.2	26.9	21.9
	Degraded	12.2	4.4	1.4	0.9	0.6
	940 nm (sun)	0	0.3	0.65	1.0	1.5
Narrow-bandgap sub-cell testing (530 nm 1.5 suns)	Fresh	2.1	1.7	1.8	2.0	14.4
	Degraded	1.4	0.9	0.9	0.6	0.5

Supplementary References

1. Jacobsson, T. J., et al. An open-access database and analysis tool for perovskite solar cells based on the FAIR data principles. *Nat. Energy* **7**, 107−115 (2022).
2. Kuang, Y., et al. Solar-driven, highly sustained splitting of seawater into hydrogen and oxygen fuels. *Proc. Natl. Acad. Sci.* **116**, 6624–6629 (2019).
3. Wang, Y., et al. Direct Solar Hydrogen Generation at 20% Efficiency Using Low-Cost Materials. *Adv. Energy Mater.* **11**, 2101053 (2021).
4. Park, H., et al. Water Splitting Exceeding 17% Solar-to-Hydrogen Conversion Efficiency Using Solution-Processed Ni-Based Electrocatalysts and Perovskite/Si Tandem Solar Cell. *ACS Appl. Mater. Interfaces* **11**, 33835–33843 (2019).
5. Luo, J., et al. Water photolysis at 12.3% efficiency via perovskite photovoltaics and Earth-abundant catalysts. *Science* **345**, 1593−1596 (2014).
6. Wang, J., et al. Halide homogenization for low energy loss in 2-eV-bandgap perovskites and increased efficiency in all-perovskite triple-junction solar cells. *Nat. Energy* **9**, 70–80 (2024).
7. Oswald, S., Reiche R. Binding state information from XPS depth profiling: capabilities and limits. *Applied Surface Science* **179**, 307–315 (2001).
8. Demchenko, I. N., Melikhov Y., Syryanyy Y., Zaytseva I., Konstantynov P., Chernyshova M. Effect of argon sputtering on XPS depth-profiling results of Si/Nb/Si. *J. Electron Spectrosc. Relat. Phenom.* **224**, 17–22 (2018).